ROYAL SOCIETY
OF CHEMISTRY

Check for updates

In situ templating synthesis of mesoporous Ni–Fe electrocatalyst for oxygen evolution reaction†

Ya Wang,‡ Jun Yu,‡ Yanding Wang, Zhuwen Chen, [ID] Lei Dong, Rongming Cai, Mei Hong, [ID]* Xia Long* and Shihe Yang [ID]*

Low-cost and efficient electrocatalysts with high dispersion of active sites and high conductivity are of high importance for oxygen evolution reaction (OER). Herein, we use amorphous mesoporous fumed silica (MFS) as a skeleton material to disperse Ni^{2+} and Fe^{3+} through a simple impregnation strategy. The MFS is *in situ* etched away during the OER process in 1 M KOH to prepare a stable mesoporous Ni–Fe electrocatalyst. The high specific surface area and abundant surface silanol groups in the mesoporous fumed silica afford rich anchor sites for fixing metal atoms *via* strong chemical metal–oxygen interactions. Raman and XPS investigations reveal that Ni^{2+} formed covalent bonds with surface Si–OH groups, and Fe^{3+} inserted into the framework of fumed silica forming Fe–O–Si bonds. The mesoporous Ni–Fe catalysts offer high charge transfer abilities in the OER process. When loaded on nickel foam, the optimal 2Ni1Fe-MFS catalyst exhibits an overpotential of 270 mV at 10 mA cm^{-2} and a Tafel slope of 41 mV dec^{-1}. Notably, 2Ni1Fe-MFS shows a turnover frequency value of 0.155 s^{-1} at an overpotential of 300 mV, which is 80 and 190 times higher than that of the state-of-the-art IrO_2 and RuO_2 catalysts. Furthermore, 2Ni1Fe-MFS exhibits 100% faradaic efficiency, large electrochemically active surface area, and good long-term durability, confirming its outstanding OER performance. Such high OER efficiency can be ascribed to the synergistic effect of high surface area, dense metal active sites and interfacial conductive path. This work provides a promising strategy to develop simple, cost-effective, and highly efficient porous Ni–Fe based catalysts for OER.

Introduction

Hydrogen is an environmentally friendly energy source with zero CO_2 emission when releasing its energy content by reacting with oxygen to form water.[1–3] Currently, hydrogen is mainly produced from natural gas, naphtha, oil and other non-renewable resources by thermal processes.[4] These processes can cause serious environmental pollution. Potentially, hydrogen can also be obtained by sustainable strategies through the electrolysis of water applying electricity generated from renewable energy sources, such as wind and solar energy.[5] However, the efficiency of electrochemical water-splitting suffers from the sluggish kinetics of OER, since the reaction is a four-electron transfer process, and high overpotentials are required.[6–11] Thus, it is highly desired to explore active OER electrocatalysts to reduce the energy barrier.

Ir- and Ru-based materials exhibit state-of-the-art OER catalytic activity, but the high price of such rare metals always limits its wide application.[12] Currently, earth-abundant and low-cost transition metal materials (Ni, Fe, Mn, Co, *etc.*) have been developed and they exhibit high activity under alkaline conditions.[13–16] Usually, these catalysts with higher surface areas exhibit enhanced active sites and possess much higher OER efficiency.

Great efforts have been devoted to the construction of large surface area electrocatalysts to facilitate OER.[17–20] One way is to prepare low-dimensional structures (1D nanorods and 2D nanoflakes). Mu *et al.* has reported a Co–N_x/C nanorod array derived from 3D zeolitic-imidazolate frameworks nanocrystals, its superior oxygen reduction reaction (ORR) and OER catalytic activities are largely attributed to the high surface area and abundant active sites of the nanorods.[21,22] The Ni_3S_2 nanorods,[23] perovskite nanorods,[24] $NiFe_2O_4$ nanorods,[25] $CoMoO_4$ nanorods,[26] iron phosphide (FeP) nanorods[27] and Ag-based nanocomposite[22] also showed outstanding catalytic activity toward the OER. Fang *et al.* developed a pulsed laser surface modification strategy to synthesis ultra-small Ir spheres (*ca.* 2 nm) around the IrO_2 core, which increased the electrochemical surface area and electrical conductivity of the electrocatalyst.[28] Oxygen evolution can be electrocatalyzed by nanoflake

State Key Laboratory of Chemical Oncogenomics, Guangdong Provincial Key Laboratory of Nano-Micro Materials Research, School of Chemical Biology & Biotechnology, Peking University Shenzhen Graduate School (PKUSZ), Shenzhen 518055, P. R. China. E-mail: xialong@pku.edu.cn; chsyang@pku.edu.cn; hongmei@pku.edu.cn; Fax: +86 755 26033174; Tel: +86 755 26032970

† Electronic supplementary information (ESI) available. See DOI: 10.1039/d0ra03111a

‡ These authors contributed equally to this work.

electrode, such as NiSe,[29] Fe_2O_3,[30] mesoporous $NiCo_2O_4$ (ref. 31) nanoflakes. Transition metal based layered double hydroxides (TM LDHs)[32–35] also exhibit exceptional OER performance. The 2D layer structure helps to expose and stabilize active sites.

Alternatively, one simple and scalable way to prepare electrocatalysts is to facilely load metals onto porous substrates, either as 3D skeleton or as sacrificial template.[36–39] The hierarchical porous structure doped with dispersed and activated catalysts can directly provide easy access to available active site. Various types of templates, such as carbon,[2,40,41] silica[42–44] and inorganic salt[45] have been investigated to construct the porous structure in electrocatalyst. Fang *et al.* employed ordered mesoporous carbon (OMC) to support nickel oxide and cobalt oxide nanocomposites as a highly efficient electrocatalyst.[2] In particular, the rock salt type $NiCo_2O_3$@OMC exhibits a small overpotential of 281 mV at the current density of 10 mA cm^{-2} and a moderate Tafel slope of 96.8 mV dec^{-1}. Yang *et al.* employed porous substrate including graphene, carbon nanotubes, C_3N_4, $CaCO_3$, and porous organic polymers, to physically adsorbed metal ions as efficient OER catalysts.[46]

Ordered mesoporous $NiCo_2O_4$ has been synthesized by using highly ordered mesoporous KIT-6 silica templates, its porous structure with large specific surface area, interconnected pores and controllable pore sizes leads to the excellent performance in OER and ORR.[43] Mesoporous silica of SBA-15 molecular sieve can also be used as hard template for preparing morphology controlled IrO_2 nanomaterial as high activity OER catalyst.[44] Recently, Cai *et al.* employed an ingeniously designed photocorrosion method using a modified coordinating etching of Cu_2O as a template to synthesize the homogeneous amorphous nanocages of Cu–Ni–Fe hydr(oxy)oxide as a highly efficient electrocatalyst.[47] However, the templates employed are either too expensive or the template removal method is too complicated. It would be desirable to combine cheap porous templates and easy template removal method to achieve a highly efficient electrocatalyst in a facile and scalable way.

In this work, we use commercial mesoporous fumed silica (MFS) as 3D hierarchical supports to anchor Ni^{2+} and Fe^{3+}, then Ni–Fe–O mesoporous electrocatalyst was formed by using *in situ* etching process of MFS skeleton during OER process in 1 M KOH. The synthesis route of Ni–Fe–O electrocatalyst is illustrated in Fig. 1a. The mesoporous fumed silica exhibits high specific surface area, branched mass fractal structure, and rich surface silanol groups.[48] These compositional and structural properties value significant advantages so that the Ni and Fe could anchor on MFS, affording stable mesoporous Ni–Fe–O electrocatalyst *via in situ* etching. This mesoporous electrocatalyst showed high OER efficiency due to advanced charge transfer ability and large electrochemical active surface area.

Experimental

Synthesis of Ni and Fe anchored mesoporous fumed silica

Mesoporous fumed silica support was purchased from Degussa. Nickel(II) chloride hexahydrate ($NiCl_2 \cdot 6H_2O$) and iron(III) chloride hexahydrate ($FeCl_3 \cdot 6H_2O$) were analytical reagent (AR) grade and obtained from Adamas. All chemicals were used without further purification. For the synthesis of Ni and Fe anchored mesoporous fumed silica (collectively named as NiFe-MFS), 0.6 g of fumed silica was stirred with 30 mL of x M $NiCl_2 \cdot 6H_2O$ and $(0.1 - x)$ M $FeCl_3 \cdot 6H_2O$ aqueous solution at 40 °C for 2 h. The product was obtained by filtration and washing with water three times, then drying at 70 °C more than 12 h. A series of NiFe-MFS catalysts were synthesized with different mole ratio of metal-ion aqueous solutions, and the resulting materials are designated as Ni-MFS (0.1 M $NiCl_2 \cdot 6H_2O$), 8Ni1Fe-MFS (0.088 M $NiCl_2 \cdot 6H_2O$ and 0.011 M $FeCl_3 \cdot 6H_2O$), 4Ni1Fe-MFS (0.08 M $NiCl_2 \cdot 6H_2O$ and 0.02 M $FeCl_3 \cdot 6H_2O$), 2Ni1Fe-MFS (0.066 M $NiCl_2 \cdot 6H_2O$ and 0.033 M $FeCl_3 \cdot 6H_2O$), 1Ni1Fe-MFS (0.05 M $NiCl_2 \cdot 6H_2O$ and 0.05 M $FeCl_3 \cdot 6H_2O$), 1Ni2Fe-MFS (0.033 M $NiCl_2 \cdot 6H_2O$ and 0.066 M $FeCl_3 \cdot 6H_2O$) and Fe-MFS (0.1 M $FeCl_3 \cdot 6H_2O$) respectively. In comparison, 0.6 g different silica with various particle size and pore size were stirred with 30 mL aqueous solution containing 0.066 M $NiCl_2 \cdot 6H_2O$ and 0.033 M $FeCl_3 \cdot 6H_2O$ at 40 °C for 2 h to prepare reference samples, named as 2Ni1Fe-SiO_2 sphere-10/100 (the particle size was 10 μm and pore size was 100 nm), 2Ni1Fe-SiO_2 sphere-30/300 (the particle size was 30 μm and pore size was 300 nm), 2Ni1Fe-SiO_2 sphere-30/1000 (the particle size was 30 μm and pore size was 1000 nm), 2Ni1Fe-silica sand (nonporous SiO_2 quartz sand). These silica spheres were supplied by Suzhou Nanomicro Technology Co., Ltd.

Catalyst characterization

The nanostructure of the samples was investigated by transmission electron microscopy (TEM), high-resolution TEM (HRTEM) and selected area electron diffraction (SAED) (Tecnai G2 F20 STWIN, 200 kV). The Ni, Fe, Si and O element distribution was measured by energy-dispersive X-ray (EDX) mapping. The crystallinity of the samples was studied by X-ray diffraction (XRD, Bruker D8 Advance diffractometer with Cu Kα). The morphology of the samples was analyzed by field emission scanning electron microscopy (FE-SEM, ZEISS Supra 55, 5 kV). The binding energy of elements was analyzed by X-ray photoelectron spectroscopy (XPS, ESCALAB 250Xi). Raman spectroscopy was performed on ReactRaman 785 equipped with a 785 nm laser excitation (Mettler Toledo ReactRaman 785). Elemental contents of the samples were measured by inductively coupled plasma-atomic emission spectrometer (ICP-AES, Arcos II MV). The Brunauer–Emmett–Teller (BET) surface area and porous structure of the samples were investigated using nitrogen gas adsorption–desorption isotherms at −196 °C on a Micromeritics Tristar II 3020 v1.03 analyzer. The powder samples were degassed at 180 °C *in vacuo* for at least 8 h before measurements. The BET surface areas were calculated from the adsorption data from $0.01 < P/P_0 < 0.35$ in the range of linearity according to IUPAC recommendation.[49] The mesopore size distributions were determined from the desorption data using the Barrett–Joyner–Halenda (BJH) model.

Electrochemical analysis

Electrochemical measurements were carried out in a three-electrode system at 25 °C in 1 M KOH (CHI760E). A Pt wire
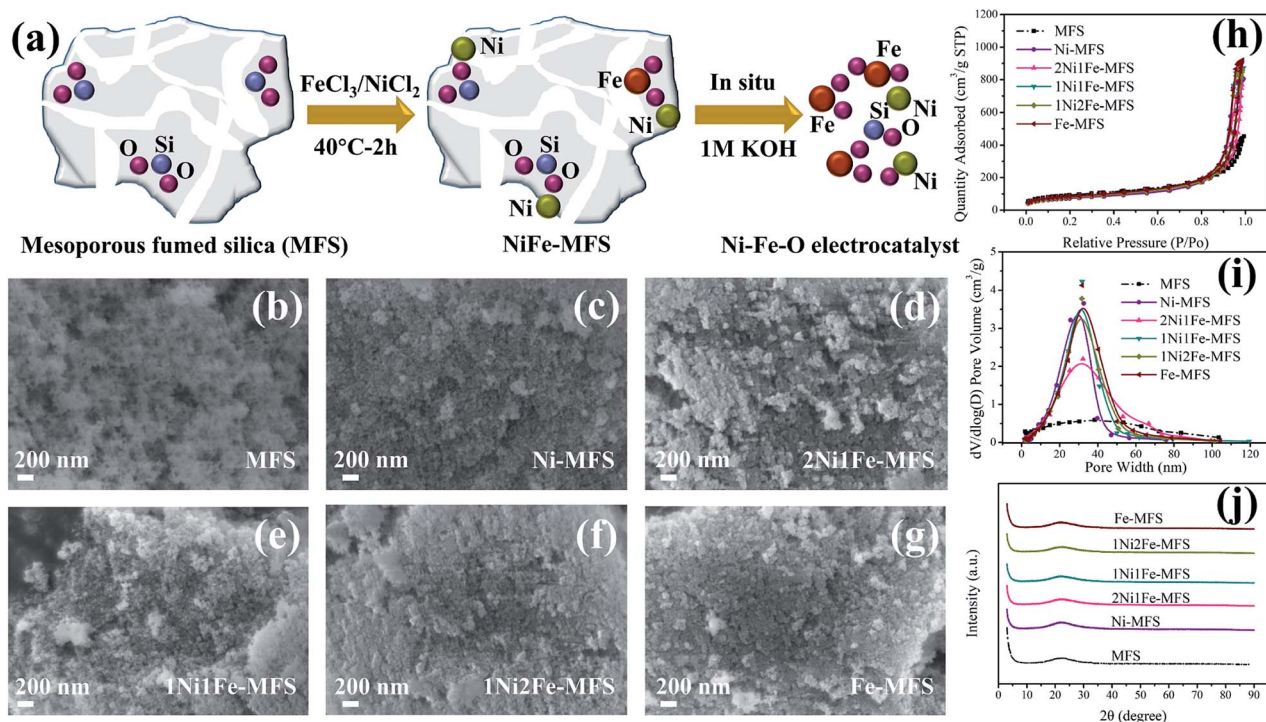
Fig. 1 Characterization of template MFS and the as-synthesized NiFe-MFS samples. (a) The synthesis route of Ni−Fe−O electrocatalysts, (b−g) SEM images, (h) N$_2$ adsorption−desorption isotherms, (i) BJH pore size distribution curves, and (j) XRD patterns of MFS and various NiFe-MFS samples.

was used as the counter electrode and an Ag/AgCl electrode was used as reference electrode. The preparation of the working electrode was as follows: 2 mg of catalyst was dispersed ultrasonically in 400 μL of water, and then 400 μL of 4 wt% PTFE was added before sonication for 30 min for forming the catalyst ink. Then the catalyst ink was dropped onto a carbon cloth or nickel foam (1 cm × 1 cm), and dried at room temperature overnight. The potentials measured were converted to the reversible hydrogen electrode (RHE) scale according to the eqn (1):

$$E(vs.\ \mathrm{RHE}) = E(\exp) + E(\mathrm{Ag/AgCl}) + 0.059 \times \mathrm{pH} \quad (1)$$

The work electrode underwent a cyclic voltammetry (CV) activation at a scan rate of 10 mV s^{-1} for 40 times. Then linear sweep voltammetry (LSV) was carried out at 5 mV s^{-1} and the Tafel plots were measured at 1 mV s^{-1}. LSV polarization curves were 95% internal resistance (iR) corrected. The turnover frequency (TOF) value is calculated from the eqn (2):

$$\mathrm{TOF} = SI/(4nF) \quad (2)$$

where S is the surface area of the working electrode, I is the measured current density at the overpotential of 0.3 V, n is the moles of active materials (assuming that both Ni and Fe are active sites in OER) loaded on the electrode,[2,50] the content of Ni and Fe was calculated by using the measured result of ICP. F is the Faraday constant (96 485 C mol^{-1}).

The electrochemically active surface area (ECSA) was calculated by cyclic voltammetry method using the following formula

ECSA = $C_{\mathrm{dl}}/C_{\mathrm{s}}$, where C_{dl} is the double-layer capacitance, C_{s} is the specific capacitance assumed to be 0.040 mF cm^{-2} in this work.[13]

The long term stability was conducted by chronopotentiometry (CP) under a constant current density of 10 and 50 mA cm^{-2}. Electrochemical impedance spectroscopy (EIS) analysis was conducted at 1.52 V vs. RHE with an AC voltage of 5 mV from 100 kHz to 0.01 Hz. Faradaic efficiency is calculated from the eqn (3):

$$\mathrm{Faradaic\ efficiency} = nZF/(It) \quad (3)$$

where n is the moles of O$_2$ evolution, Z is the number of electrons that are needed to produce one O$_2$ molecule, F is the Faraday constant (96 485 C mol^{-1}), I is the current density (A), t is the reaction time (s). Here we used a constant current of 20 mA for 60 min, and in-process samples were taken at 10 min interval by collecting 1 mL of the gas from the reactor which was analyzed using gas chromatograph equipped with a thermal conductivity detector (TCD, GC-2014C, SHIMADZU).

Results and discussion

Physicochemical characterization

The Ni and Fe anchored mesoporous fumed silica (NiFe-MFS) catalysts were prepared via a simple and scalable impregnation method at 40 °C. The morphology, crystal structure, BET surface area and pore structure of the NiFe-MFS samples as well as the bare mesoporous fumed silica (MFS) were analyzed by

scanning electron microscopy (SEM), X-ray diffraction (XRD) and nitrogen gas adsorption–desorption measurements, and the results are shown in Fig. 1 and Table 1. As illustrated in Fig. 1b, SEM images show that the pristine fumed silica are powder materials with porous structure. They remain porous after impregnation with Ni or Fe aqueous solution (Fig. 1c–g). XRD results (Fig. 1j) indicated that all the materials including MFS and Ni and Fe anchored MFS are amorphous. The mesoporous structure of MFS and all NiFe-MFS was confirmed using N_2 adsorption–desorption measurements. All of the samples show a type IV isotherm and an H1 hysteresis loops[51] (Fig. 1h), and the Barrett–Joyner–Halenda (BJH) distribution of pore size reflects the mesopores of $\sim$30 nm (Fig. 1i). Compared to the pristine MFS, the Ni and Fe anchored NiFe-MFS samples exhibited much narrower pore size distribution and a smaller peak pore diameter, confirming the slight aggregation of the silica that leads to sharpening the mesopore size distribution caused by impregnation as observed by SEM images. The pore volume of NiFe-MFS is nearly twice of that of MFS (Table 1), while the BET surface area of NiFe-MFS (250–290 m^2 g^{-1}) is lower compared with that of the pristine fumed silica (314 m^2 g^{-1}), indicating preservation of the porous structure. The size of the nanoparticle might have increased leading to larger pore volume, pore size and smaller surface area. The SEM, XRD and N_2 adsorption–desorption results have proved that the mesoporous architecture of the MFS support remains unaffected after metal anchoring, and NiFe-MFS samples possess much larger mesoporous volume even after impregnation of Ni and Fe catalysts. These mesoporous materials as electrodes can not only enhance molecular transport properties, but also increase the accessibility of reaction-relevant species to the active sites. These important features of porous structure make them very promising catalysts for OER electrocatalytic applications.[52]

The microstructure of the 2Ni1Fe-MFS and 1Ni2Fe-MFS samples was investigated using TEM and HRTEM (Fig. 2 and S1†). Both the 2Ni1Fe-MFS and 1Ni2Fe-MFS samples show skeleton composed of SiO_2 particles with a size of $\sim$20 nm, and these nanoparticles are stacked together forming branches (Fig. 2b and S1a†). The HRTEM image (Fig. 2a) and the corresponding selected area electronic diffraction (SAED) patterns (Fig. 2c) of the 2Ni1Fe-MFS sample barely show lattice fringes and diffraction spots, indicating that the sample is mostly
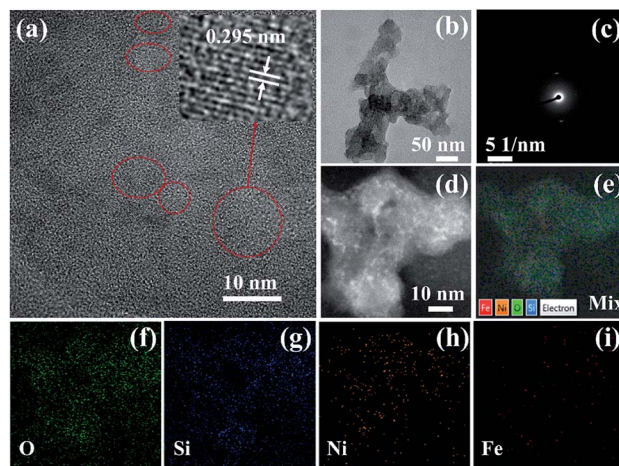

Fig. 2 Characterization of the 2Ni1Fe-MFS MFS sample. (a) HRTEM image with the inserted lattice fringes, (b) TEM image, (c) SAED pattern, (d) HAADF-STEM image and (e–i) EDX elemental mapping images of O, Si, Ni, and Fe elements.

amorphous with little nanocrystals, its lattice fringe is about 0.295 nm, which corresponds to the (206) plane of α-Fe_2O_3 (PDF#25-1402). However, the HRTEM (Fig. S1b†) and the corresponding SAED pattern (Fig. S1c†) of 1Ni2Fe-MFS show it is an amorphous state. The metals are uniformly distributed within the support MFS, evidenced by HAADF-STEM image (Fig. 2d) and EDX mapping (Fig. 2e–i). The content of Fe and Ni in 2Ni1Fe-MFS and 1Ni2Fe-MFS samples has been obtained by ICP-AES (Table S1†). 2Ni1Fe-MFS sample was prepared with a Ni and Fe loading of 1.01 and 0.94 wt%, and the Ni and Fe loading in 1Ni2Fe-MFS were 0.50 and 1.67 wt% respectively.

The surface composition and surface chemical state of all samples were studied by X-ray photoelectron spectroscopy (XPS). The XPS survey spectra (Fig. S2†) illustrate the existence of Si and O, while almost no Ni and Fe could be detected because of the low loading of Ni and Fe in these samples. The presence of Ni and Fe in fumed silica support was confirmed in the high-resolution XPS (HR-XPS) spectra (Fig. 3c and d) and the corresponding element composition was shown in Table S2.† The atomic content of Ni was found to be less than 0.7%, and Fe atomic content was $\sim$1%. The atomic ratio of Ni/Fe decreased with the decreasing Ni concentration of the impregnation solution. XPS experiment revealed the surface concentration of Ni and Fe, while ICP-AES showed the bulk content of the elements. It was found that the Ni and Fe contents on the surface were higher than those in the bulk (Table S3†), indicating that more Ni and Fe distributed on the surface than within the MFS nanoparticle support. The HR-XPS spectra of the Ni shows two distinct peaks of Ni $2p_{3/2}$ and $2p_{1/2}$ around 856.6 eV and 874.3 eV, along with a satellite peak at 862.4 eV (Fig. 3c). The obtained binding energies well agreed with those reported in literature,[47] which were ascribed to the binding energy of Ni^{2+}. Meanwhile, the Fe 2p level exhibits two peaks at 711.7 and 725.3 eV, which were assigned to the Fe $2p_{3/2}$ and $2p_{1/2}$ states of Fe^{3+} (Fig. 3d).[47] The O 1s peak of the pristine fumed silica is at 533.1 eV, which is assigned to the oxygen in the form

Table 1   BET surface area and pore volume of MFS and NiFe-MFS

Sample	BET surface area (m^2 g^{-1})	Pore volume (m^3 g^{-1})		
		V_{micro}[a]	V_{meso}	V_{total}[b]
MFS	314	0.02	0.64	0.66
Ni-MFS	248	0.02	1.18	1.20
2Ni1Fe-MFS	283	0.01	0.98	0.99
1Ni1Fe-MFS	267	0.01	1.28	1.29
1Ni2Fe-MFS	266	0.01	1.24	1.25
Fe-MFS	288	0.01	1.34	1.35

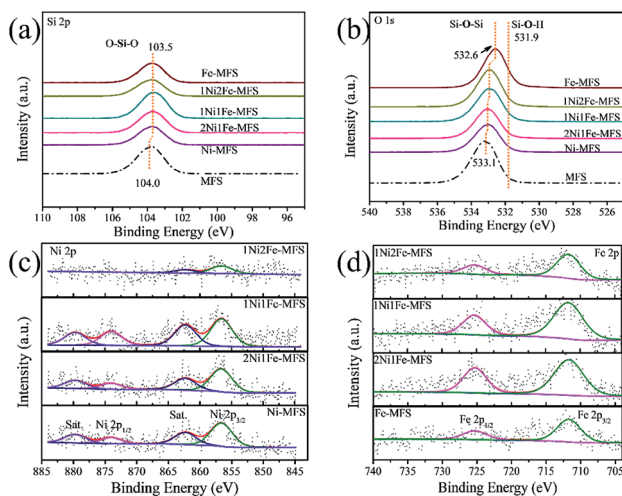[a] t-plot micropore volume. [b] Total pore volume calculated as the amount of N_2 adsorbed at $P/P_0 = 0.98$.

Fig. 3 High-resolution XPS spectra of MFS and various NiFe-MFS samples. (a) Si 2p, (b) O 1s, (c) Ni 2p, and (d) Fe 2p.

Fig. 4 Raman spectra of MFS and various NiFe-MFS samples.

of Si–O–Si.[53] The binding energy of the O 1s gradually shifted to a lower energy with increasing Fe content (Fig. 3b), reaching 532.6 eV for the solely Fe^{3+} impregnated Fe-MFS. Similarly, the Si 2p peak shows a lower binding energy for Fe-MFS (103.5 eV) in comparison with that in pristine fumed silica (104.0 eV) (Fig. 3a). This gives evidence to the electron transfer between Si/O and metal Ni or Fe. The phenomena of Ni and Fe enrichment on the surface of MFS nanoparticle and electron transfer between metals and MFS indicate that Ni and Fe are anchored onto the surface of the MFS supports rather than being adsorbed in the MFS mesoporous channels.

The tethering of the Ni/Fe transitions metals to the support fumed silica is further confirmed by Raman spectroscopy measurements. For MFS (Fig. S3†), bands at 345–450, 575, 750, 973 and 1070 cm^{-1} are observed and can be attributed to Si–O–Si network bending, D2 defect mode of the three-membered cyclosiloxane ring, Si–O–Si symmetrical stretching, surface Si–OH stretching and transverse-optical (TO) stretch of the silica network, respectively.[54–57] For the samples with relatively high Fe content (Fe-MFS, 1Ni2Fe-MFs, 1Ni1Fe-MFS) (Fig. 4), new bands at 332, 495 and 1163 cm^{-1} are observed in the Raman spectra. These bands are attributed to the framework of Fe–O–Si species. The 332 cm^{-1} Raman peak is ascribed to the O–Fe–O bending, 495 cm^{-1} is ascribed to the Fe–O–Si bending, and 1163 cm^{-1} to the Fe–O–Si asymmetric stretch mode.[55] The absence of some weak Raman bands at 345, 550, 810 and 842 cm^{-1} might be due to the stretching or bending changes in surface structure, after Fe insertion into the fumed silica structure. However, compared with the pristine fumed silica, the band at 973 cm^{-1} (surface Si–OH stretching) diminished for the relatively high Ni content samples (Ni-MFS and 2Ni1Fe-MFS), and no more new bands are observed. This means that Ni was just anchored on the surface Si–OH, not incorporated into the skeleton of the fumed silica. Combining the results from high-resolution XPS (Fig. 3) and Raman (Fig. 4) spectra, we can deduce that besides adsorption, Fe^{3+} prefers to insert into the framework of the fumed silica and forms Fe–O–Si bonding,
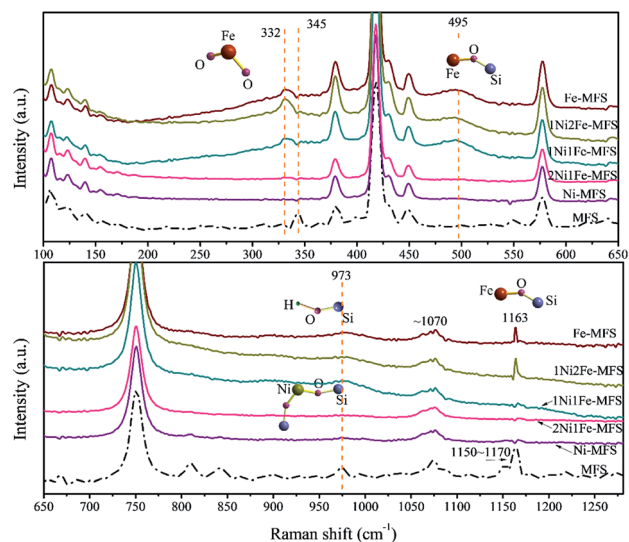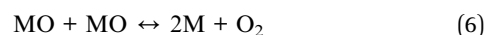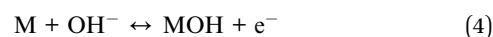
while Ni^{2+} covalently binds with surface Si–OH groups and anchors on the surface of the fumed silica. The schematic description of Ni anchoring on the surface and Fe substitution into fumed silica is shown in Scheme 1.
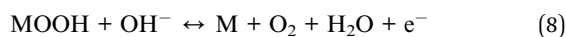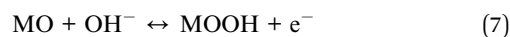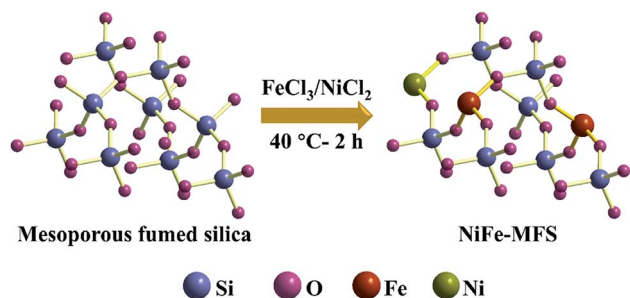
Electrocatalytic water oxidation

To evaluate the OER catalytic activities of Ni and Fe anchored MFS, the electrochemical measurements for water oxidation of these powders on carbon cloth in 1 M KOH electrolyte were carried out (Fig. 5). Fig. 5 shows the linear sweep voltammetry (LSV) curves (with *iR* compensation), Nyquist plots, and Tafel plots of 2Ni1Fe-MFS, 1Ni1Fe-MFS and 1Ni2Fe-MFS electrodes. The 2Ni1Fe-MFS modified electrode show the oxidation peak at 1.38–1.46 V *vs.* RHE, which can be assigned to the conversion of Ni^{2+} to Ni^{3+}, indicating the formation of NiOOH during the OER test.[2,58] Ni^{3+} is also the active species for OER. The overpotentials at 10 mA cm^{-2} were 310, 385 and 446 mV for 2Ni1Fe-MFS, 1Ni1Fe-MFS and 1Ni2Fe-MFS, respectively. Their corresponding Tafel slopes were 42, 47 and 81 mV dec^{-1}. The decrease of the overpotential and Tafel slope means that Ni and Fe anchoring at an optimal content enhanced OER efficiency and improved reaction kinetics of the electrocatalytic process.

According to the literatures,[2,58–60] the reaction pathways of OER in alkaline media are generally composed of the following steps:

$$M + OH^- \leftrightarrow MOH + e^- \tag{4}$$

$$MOH + OH^- \leftrightarrow MO + H_2O + e^- \tag{5}$$

$$MO + MO \leftrightarrow 2M + O_2 \tag{6}$$

or

$$MO + OH^- \leftrightarrow MOOH + e^- \tag{7}$$

$$MOOH + OH^- \leftrightarrow M + O_2 + H_2O + e^- \tag{8}$$

Scheme 1   The proposed formation process of NiFe-MFS.

Fig. 6   (a) 95% *iR*-compensated polarization curves, (b) Tafel plots of 2Ni1Fe-MFS, IrO$_2$ and RuO$_2$ modified nickel foam electrodes.

In which M refers to the active site of a catalyst, MOH, MO, and MOOH represent the intermediate species.

Due to different chemical characters of nickel and iron ions, the formed NiFe-MFS with various Ni/Fe ratios would show distinct adsorption–desorption properties, leading to different OER pathways. Actually, it has been reported that Fe could stabilize MO, while Ni would promote O–O coupling.[59] Herein, 2Ni1Fe-MFS and 1Ni1Fe-MFS with relatively low Ni/Fe ratio would likely to go through the O–O coupling step to form O$_2$ (step 6), leading to small Tafel slopes of 42 mV dec^{-1} and 47 mV dec^{-1}, respectively. However, with the increase of Fe that could stabilize MO intermediates, the nucleophilic attack of OH$^-$ to MO to form MOOH (step 7) would be the rate-determining step for OER on 1Ni2Fe-MFS, resulting in a large Tafel value of 81 mV dec^{-1}.

In the meantime, the semicircle of the Nyquist plots of the 2Ni1Fe-MFS sample was smaller than that of the 1Ni1Fe-MFS and 1Ni2Fe-MFS samples (Fig. 5d), which indicated that the charge transfer kinetics of the 2Ni1Fe-MFS has been improved when Ni and Fe are anchored at an optimal content. While increasing the proportion of Ni/Fe as in the samples 4Ni1Fe-MFS and 8Ni1Fe-MFS (the Ni/Fe ratio measured by ICP-AES is shown in Table S4†), the overpotential increased although
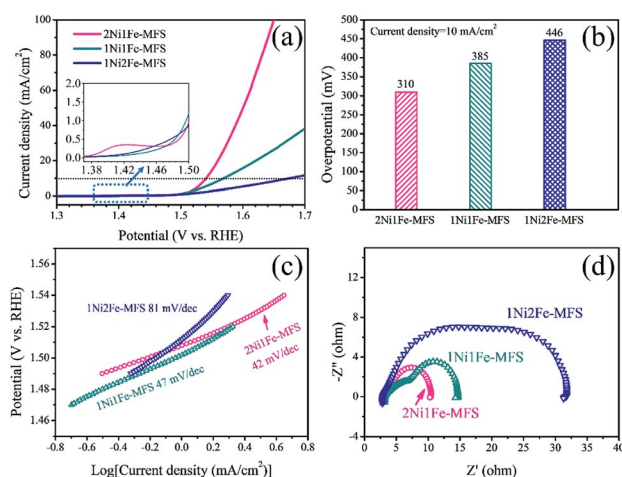
4Ni1Fe-MFS showed the relatively lowest Tafel slope of 43 mV dec^{-1} (Fig. S4†). To investigate the OER intrinsic activity of the 2Ni1Fe-MFS, 1Ni1Fe-MFS and 1Ni2Fe-MFS samples, electrochemically active surface area (ECSA) was measured and the ECSA normalized current density with potential of samples were shown in Fig. S5.† The results show that 1Ni1Fe-MFS sample possesses the highest OER intrinsic activity, while 2Ni1Fe-MFS catalyst has the larger double-layer capacitance C_{dl} and ECSA (Fig. S5e and S5f†).

We also tested the OER electrocatalytic activity of 2Ni1Fe-MFS on nickel foams that are more electrically conductive and possesses higher electrode surface area compared to those on carbon cloth electrodes. In comparison, electrodes including the commonly referred IrO$_2$ and RuO$_2$ were also prepared using the same method (see Experimental section), and their OER performance were obtained. As shown in Fig. 6, 2Ni1Fe-MFS exhibits much lower overpotential at 10 mA cm^{-2} (270 mV) on nickel foams. The overpotential is 52 and 88 mV lower than those of IrO$_2$ (322 mV) and RuO$_2$ (358 mV) on nickel foams respectively, while the OER performance by IrO$_2$ or RuO$_2$ was consistent with results from previous reports.[61–64] The Tafel slope for 2Ni1Fe-MFS is 41 mV dec^{-1}, which is also much lower than those of IrO$_2$ and RuO$_2$ on a nickel foam electrode. The

Fig. 5   (a) 95% *iR*-compensated polarization curves, (b) overpotentials at 10 mA cm^{-2}, (c) Tafel plots, and (d) Nyqusit plots of 2Ni1Fe-MFS, 1Ni1Fe-MFS and 1Ni2Fe-MFS modified carbon cloth electrodes.
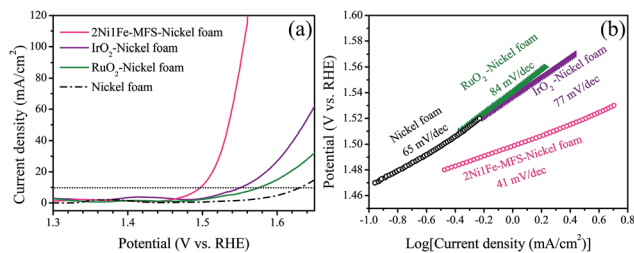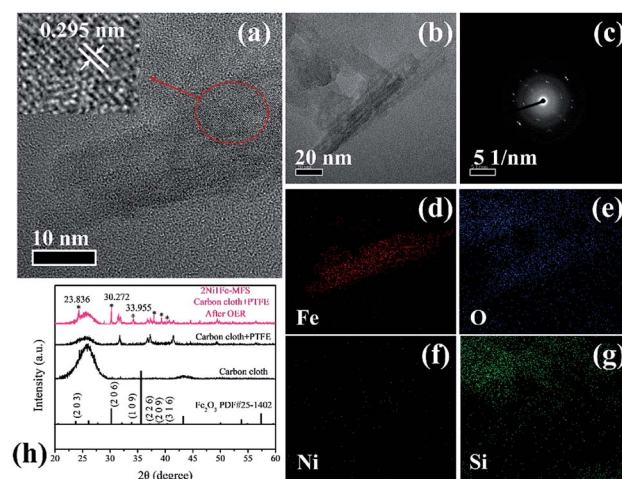

Fig. 7   (a) HRTEM image with the inserted lattice fringes, (b) TEM image, (c) SAED pattern, (d–g) EDX elemental mapping images of Fe, O, Ni, Si, and (h) XRD pattern of 2Ni1Fe-MFS (after OER) dispersed in PTFE on carbon cloth electrodes.

TOF value is 0.155 s^{-1} at the overpotential of 300 mV, which is 80 and 190 times higher than that of the state-of-art IrO$_2$ and RuO$_2$ catalyst (Table S5†).

To investigate the structure of 2Ni1Fe-MFS after OER reaction, TEM, XRD and XPS of 2Ni1Fe-MFS on carbon cloth electrode were carried out. As shown in Fig. 7, the sample showed crystal plane spacing of 0.295 nm (Fig. 7a). The element distribution in Fig. 7d–g shows the presence of Fe and O with a small amount of Ni in the structure, and the Si element disappeared confirming the completeness of the *in situ* etching. Si is mainly distributed in the adjacent binder. The XRD pattern shows that Fe and O in the sample constitute the Fe$_2$O$_3$ structure, and the lattice spacing corresponds to the (206) plane. The XPS spectra of 2Ni1Fe-MFS after OER reaction in 1 M KOH solution are displayed in Fig. S6.† As shown in Fig. S6,† the Si content in the 2Ni1Fe-MFS sample decreased significantly, and the signal strength of Ni and Fe increased compared with pristine 2Ni1Fe-MFS. This means that Si element was etched in a strong alkaline solution, exposing Ni and Fe elements which were the OER active centers.

To further study the structure of 2Ni1Fe-MFS after OER reaction, 2Ni1Fe-MFS on carbon cloth electrode after 30 cycles of CV was analyzed using XPS. The CV result (Fig. S7a†) shows the oxidation peak of Ni^{2+} to Ni^{3+} for 2Ni1Fe-MFS, again indicating the formation of oxyhydroxides during the OER test. It can be clearly found that after 30 cycles of the CV, the Si element in the 2Ni1Fe-MFS sample has been etched away (Fig. S7b†). In order to investigate the pore structure after Si etching in the sample, powdery 2Ni1Fe-MFS sample was immersed in a 1 M KOH solution for 20 minutes, then centrifuged, washed and dried to obtain powder Ni–Fe–O sample. The nitrogen gas adsorption–desorption result showed that 2Ni1Fe-MFS was still a mesoporous structure even after Si etching process (Fig. S7c and S7d†). The pore volume of etched 2Ni1Fe-MFS is 0.43 m^3 g^{-1}, and the BET surface area is 58 m^2 g^{-1}. Compared with that of the pristine 2Ni1Fe-MFS (pore volume is 0.99 m^3 g^{-1}, BET surface area is 283 m^2 g^{-1}), the reduction of the specific surface area and pore volume in the sample is mainly due to removal of the Si framework structure, but the Ni–Fe–O sample after etching still has a mesoporous structure with mesopore width centered at 26 nm, which is a guarantee of its excellent OER performance.

In order to investigate the relationship between porous structure of silica sacrificial agent and OER performance, we selected different silica materials with various particle and pore size to anchor Ni and Fe. The diameters of the silica microspheres are 10, 30, and 30 μm, respectively, and the corresponding macropore diameters are 100, 300, and 1000 nm, respectively. These samples are named according to their particle size and pore size: 2Ni1Fe–SiO$_2$ sphere-10/100, 2Ni1Fe–SiO$_2$ sphere-30/300 and 2Ni1Fe–SiO$_2$ sphere-30/1000. Non-porous quartz sand was also selected for comparison. SEM images of these samples are shown in Fig. S8.† Their N$_2$ adsorption–desorption isotherms (Fig. 8a) revealed the mesoporous distribution (Fig. 8b). The mesopore sizes of samples 2Ni1Fe–SiO$_2$ sphere-10/100 and 2Ni1Fe–SiO$_2$ sphere-30/300 were 20 and 40 nm, and samples 2Ni1Fe–SiO$_2$ sphere-30/1000
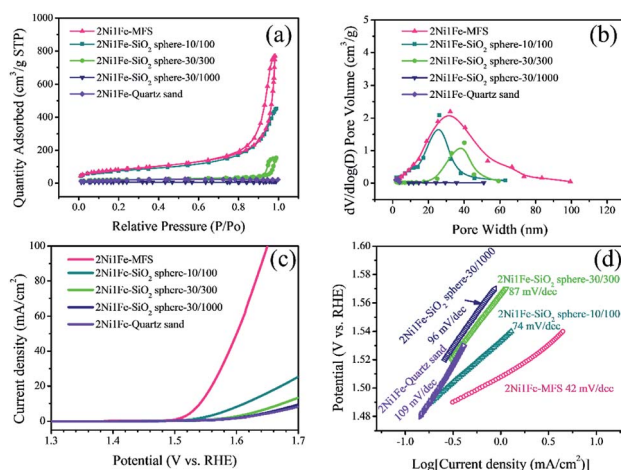

Fig. 8 (a) N$_2$ adsorption–desorption isotherms, (b) BJH pore size distribution curves, (c) 95% *iR*-compensated polarization curves, and (d) Tafel plots of 2Ni1Fe-MFS, 2Ni1Fe–SiO$_2$ sphere-10/100, 2Ni1Fe–SiO$_2$ sphere-30/300, 2Ni1Fe–SiO$_2$ sphere-30/1000 and 2Ni1Fe-quartz sand on carbon cloth electrodes.

had almost no mesoporous structure (Fig. 8b and Table S6†). The adsorption amount of nitrogen decreased with the increase of particle size and pore size (Fig. 8a). It could be seen from the comparative polarization curves and Tafel plots that the porous structure of the SiO$_2$ skeleton is critical in promoting the sample OER performance, as the overpotential at 10 mA cm^{-2} and Tafel slope decreased monotonically with the increase of 2Ni1Fe–SiO$_2$ sphere particle size and pore size. The non-porous 2Ni1Fe-quartz sand sample showed much larger overpotential at 10 mA cm^{-2} of >470 mV and higher Tafel slope of 109 mV dec^{-1} (Fig. 8c and d), while those obtained from the mesoporous fumed silica sample of 2Ni1Fe-MFS were only 310 mV and 42 mV dec^{-1} respectively, after the same alkaline etching. Thus, it is the porous structure of mesoporous fumed silica that provides anchoring positions for the metal elements and allows for well dispersed catalytic sites, enabling synergistic effects of high surface area and electroactive metals, which is a huge advantage in the OER reaction.

The faradic efficiency (FE) and stability are important factors to evaluate the practical implementation potential of an OER catalyst. Herein, the FE of the OER for 2Ni1Fe-MFS is found to be ~100% at 20 mA (Fig. S9†), suggesting its high energy conversion efficiency. Long-term stability of the electrocatalyst was confirmed by the chronopotentiometry (CP) of the 2Ni1Fe-MFS (Fig. 9a) at 10 and 50 mA cm^{-2} for 100 h. The sustained current applied to the catalyst electrode almost did not change the polarization curve (Fig. 9b), indicative to almost no change in charge transfer and reaction kinetics. The semicircle of the Nyquist plot for 2Ni1Fe-MFS sample (Fig. 9c) decreased after CP testing, indicating improved charge transfer abilities. And the slight increase of the Tafel slope (Fig. 9d) suggest a little retardance of reaction kinetics. Note that even after long-term electrical operation, the Tafel slope of the 2Ni1Fe-MFS catalyst was still smaller than those of IrO$_2$ and RuO$_2$ electrodes,
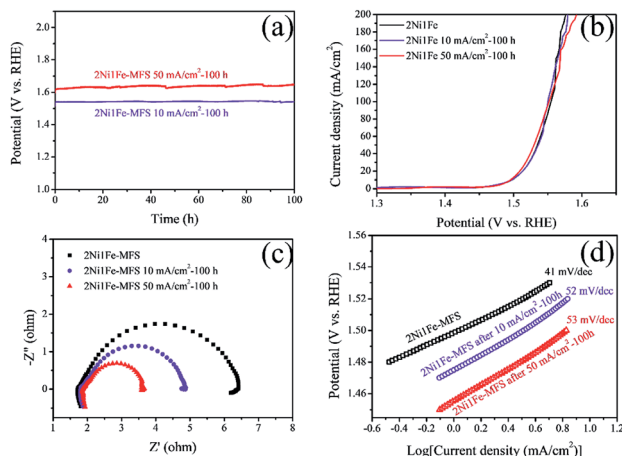
Fig. 9 (a) Long-term stability test of 2Ni1Fe-MFS, (b) 95% *iR*-compensated polarization curves, (c) Nyquist plots and (d) Tafel plots of 2Ni1Fe-MFS on nickel foam electrode before and after long-term stability tests.

confirming that the 2Ni1Fe-MFS catalyst not only possesses high efficiency but also exhibits good stability during OER process.

Conclusions

In conclusion, a cost-effective mesoporous electrocatalyst with high OER efficiency was fabricated by facile and robust anchoring of Ni and Fe on commercial fumed silica as sacrificial hard template removed through *in situ* alkaline etching. The 2Ni1Fe-MFS (1.01 wt% Ni and 0.94 wt% Fe) sample exhibits an overpotential of 310 mV at 10 mA cm^{-2} and a Tafel slope of 42 mV dec^{-1} with 100% faradaic efficiency on carbon cloth, the overpotential is 270 mV at 10 mA cm^{-2} on nickel foam with Tafel slope of 41 mV dec^{-1}. The mesoporous fumed silica provides a large surface area and skeleton for the transition metal anchoring, the mesoporous Ni–Fe electrocatalyst was formed after *in situ* Si etching process in 1 M KOH. All these factors contributed to the superior catalytic performance in OER, supported by the high turnover frequency value, high charge transfer ability, and long-term stability of the 2Ni1Fe-MFS sample. These findings highlight the possibility of using mesoporous fumed silica as a novel skeleton to construct porous OER electrocatalyst. Transition metals like active Ni and Fe species can be readily anchored into the porous structure of fumed silica with high stability through a simple and scalable impregnation method.

Conflicts of interest

There are no conflicts to declare.

Acknowledgements

References

1 J. Wang, W. Cui, Q. Liu, Z. Xing, A. M. Asiri and X. Sun, Recent progress in cobalt-based heterogeneous catalysts for electrochemical water splitting, *Adv. Mater.*, 2016, **28**, 215–230.

2 Y. Zhang, X. Wang, F. Luo, Y. Tan, L. Zeng, B. Fang and A. Liu, Rock salt type NiCo$_2$O$_3$ supported on ordered mesoporous carbon as a highly efficient electrocatalyst for oxygen evolution reaction, *Appl. Catal. B Environ.*, 2019, **256**, 117852.

3 W. Zhong, S. Shen, M. He, D. Wang, Z. Wang, Z. Lin, W. Tu and J. Yu, The pulsed laser-induced Schottky junction *via in situ* forming Cd clusters on CdS surfaces toward efficient visible light-driven photocatalytic hydrogen evolution, *Appl. Catal. B Environ.*, 2019, **258**, 117967.

4 L. Lin, W. Zhou, R. Gao, S. Yao, X. Zhang, W. Xu, S. Zheng, Z. Jiang, Q. Yu, Y.-W. Li, C. Shi, X.-D. Wen and D. Ma, Low-temperature hydrogen production from water and methanol using Pt/α-MoC catalysts, *Nature*, 2017, **544**, 80.

5 C. G. Morales-Guio, L.-A. Stern and X. Hu, Nanostructured hydrotreating catalysts for electrochemical hydrogen evolution, *Chem. Soc. Rev.*, 2014, **43**, 6555–6569.

6 L.-K. Wu, X.-Y. Liu and J.-M. Hu, Electrodeposited SiO$_2$ film: a promising interlayer of a highly active Ti electrode for the oxygen evolution reaction, *J. Mater. Chem. A*, 2016, **4**, 11949–11956.

7 A. Grimaud, O. Diaz-Morales, B. Han, W. T. Hong, Y.-L. Lee, L. Giordano, K. A. Stoerzinger, M. T. M. Koper and Y. Shao-Horn, Activating lattice oxygen redox reactions in metal oxides to catalyse oxygen evolution, *Nat. Chem.*, 2017, **9**, 457.

8 G. C. da Silva, M. R. Fernandes and E. A. Ticianelli, Activity and stability of Pt/IrO$_2$ bifunctional materials as catalysts for the oxygen evolution/reduction reactions, *ACS Catal.*, 2018, **8**, 2081–2092.

9 X. Long, W. Qiu, Z. Wang, Y. Wang and S. Yang, Recent advances in transition metal–based catalysts with heterointerfaces for energy conversion and storage, *Mater. Today Chem.*, 2019, **11**, 16–28.

10 Z. Wang, X. Long and S. Yang, Effects of metal combinations on the electrocatalytic properties of transition-metal-based layered double hydroxides for water oxidation: a perspective with insights, *ACS Omega*, 2018, **3**, 16529–16541.

11 M. Ju, X. Wang, X. Long and S. Yang, Recent advances in transition metals based compound catalysts for water splitting from the perspective of crystal engineering, *CrystEngComm*, 2020, **22**, 1531–1540.

12 Y. Shi and B. Zhang, Recent advances in transition metal phosphide nanomaterials: synthesis and applications in

hydrogen evolution reaction, *Chem. Soc. Rev.*, 2016, **45**, 1529–1541.

13 J. Yu, Q. Cao, Y. Li, X. Long, S. Yang, J. K. Clark, M. Nakabayashi, N. Shibata and J.-J. Delaunay, Defect-rich NiCeOx electrocatalyst with ultrahigh stability and low overpotential for water oxidation, *ACS Catal.*, 2019, **9**, 1605–1611.

14 N.-T. Suen, S.-F. Hung, Q. Quan, N. Zhang, Y.-J. Xu and H. M. Chen, Electrocatalysis for the oxygen evolution reaction: recent development and future perspectives, *Chem. Soc. Rev.*, 2017, **46**, 337–365.

15 J. Yu, Q. Cao, B. Feng, C. Li, J. Liu, J. K. Clark and J.-J. Delaunay, Insights into the efficiency and stability of Cu-based nanowires for electrocatalytic oxygen evolution, *Nano Res.*, 2018, **11**, 4323–4332.

16 X. Long, Z. Ma, H. Yu, X. Gao, X. Pan, X. Chen, S. Yang and Z. Yi, Porous FeNi oxide nanosheets as advanced electrochemical catalysts for sustained water oxidation, *J. Mater. Chem. A*, 2016, **4**, 14939–14943.

17 J. Qi, W. Zhang and R. Cao, Porous materials as highly efficient electrocatalysts for the oxygen evolution reaction, *ChemCatChem*, 2018, **10**, 1206–1220.

18 H. Lin, X. Long, Y. An, D. Zhou and S. Yang, Three-dimensional decoupling co-catalyst from a photoabsorbing semiconductor as a new strategy to boost photoelectrochemical water splitting, *Nano Lett.*, 2019, **19**, 455–460.

19 X. Long, H. Lin, D. Zhou, Y. An and S. Yang, Enhancing full water-splitting performance of transition metal bifunctional electrocatalysts in alkaline solutions by tailoring CeO$_2$–transition metal oxides–Ni nanointerfaces, *ACS Energy Lett.*, 2018, **3**, 290–296.

20 W. Zhong, J. Huang, S. Liang, J. Liu, Y. Li, G. Cai, Y. Jiang and J. Liu, New prelithiated V$_2$O$_5$ superstructure for lithium-ion batteries with long cycle life and high power, *ACS Energy Lett.*, 2020, **5**, 31–38.

21 I. S. Amiinu, X. Liu, Z. Pu, W. Li, Q. Li, J. Zhang, H. Tang, H. Zhang and S. Mu, From 3D ZIF nanocrystals to Co–N$_x$/C nanorod array electrocatalysts for ORR, OER, and Zn–air batteries, *Adv. Funct. Mater.*, 2018, **28**, 1704638.

22 G. Liao, J. Fang, Q. Li, S. Li, Z. Xu and B. Fang, Ag-Based nanocomposites: synthesis and applications in catalysis, *Nanoscale*, 2019, **11**, 7062–7096.

23 W. Zhou, X.-J. Wu, X. Cao, X. Huang, C. Tan, J. Tian, H. Liu, J. Wang and H. Zhang, Ni$_3$S$_2$ nanorods/Ni foam composite electrode with low overpotential for electrocatalytic oxygen evolution, *Energy Environ. Sci.*, 2013, **6**, 2921–2924.

24 Y. Zhu, W. Zhou, Y. Zhong, Y. Bu, X. Chen, Q. Zhong, M. Liu and Z. Shao, A perovskite nanorod as bifunctional electrocatalyst for overall water splitting, *Adv. Energy Mater.*, 2017, **7**, 1602122.

25 G. Liu, K. Wang, X. Gao, D. He and J. Li, Fabrication of mesoporous NiFe$_2$O$_4$ nanorods as efficient oxygen evolution catalyst for water splitting, *Electrochim. Acta*, 2016, **211**, 871–878.

26 X. Liu, Y. Yang and S. Guan, An efficient electrode based on one-dimensional CoMoO$_4$ nanorods for oxygen evolution reaction, *Chem. Phys. Lett.*, 2017, **675**, 11–14.

27 D. Xiong, X. Wang, W. Li and L. Liu, Facile synthesis of iron phosphide nanorods for efficient and durable electrochemical oxygen evolution, *Chem. Commun.*, 2016, **52**, 8711–8714.

28 W. Zhong, Z. Lin, S. Feng, D. Wang, S. Shen, Q. Zhang, L. Gu, Z. Wang and B. Fang, Improved oxygen evolution activity of IrO$_2$ by *in situ* engineering of an ultra-small Ir sphere shell utilizing a pulsed laser, *Nanoscale*, 2019, **11**, 4407–4413.

29 C. Tang, A. M. Asiri and X. Sun, Highly-active oxygen evolution electrocatalyzed by a Fe-doped NiSe nanoflake array electrode, *Chem. Commun.*, 2016, **52**, 4529–4532.

30 Z. Zhang, G. Zhou, W. Chen, Y. Lai and J. Li, Facile synthesis of Fe$_2$O$_3$ nanoflakes and their electrochemical properties for Li-air batteries, *ECS Electrochem. Lett.*, 2014, **3**, A8–A10.

31 L. Zhang, S. Zhang, K. Zhang, G. Xu, X. He, S. Dong, Z. Liu, C. Huang, L. Gu and G. Cui, Mesoporous NiCo$_2$O$_4$ nanoflakes as electrocatalysts for rechargeable Li–O$_2$ batteries, *Chem. Commun.*, 2013, **49**, 3540–3542.

32 X. Long, Z. Wang, S. Xiao, Y. An and S. Yang, Transition metal based layered double hydroxides tailored for energy conversion and storage, *Mater. Today*, 2016, **19**, 213–226.

33 Y. Wang, D. Yan, S. El Hankari, Y. Zou and S. Wang, Recent progress on layered double hydroxides and their derivatives for electrocatalytic water splitting, *Adv. Sci.*, 2018, **5**, 1800064.

34 M. Gong, Y. Li, H. Wang, Y. Liang, J. Z. Wu, J. Zhou, J. Wang, T. Regier, F. Wei and H. Dai, An advanced Ni–Fe layered double hydroxide electrocatalyst for water oxidation, *J. Am. Chem. Soc.*, 2013, **135**, 8452–8455.

35 X. Long, J. Li, S. Xiao, K. Yan, Z. Wang, H. Chen and S. Yang, A strongly coupled graphene and FeNi double hydroxide hybrid as an excellent electrocatalyst for the oxygen evolution reaction, *Angew. Chem., Int. Ed.*, 2014, **53**, 7584–7588.

36 X. Han, M. Wang, M. L. Le, N. M. Bedford, T. J. Woehl and V. S. Thoi, Effects of substrate porosity in carbon aerogel supported copper for electrocatalytic carbon dioxide reduction, *Electrochim. Acta*, 2019, **297**, 545–552.

37 Z. Zhou, A. Chen, X. Fan, A. Kong and Y. Shan, Hierarchical porous N-P-coupled carbons as metal-free bifunctional electro-catalysts for oxygen conversion, *Appl. Surf. Sci.*, 2019, **464**, 380–387.

38 C. Zhang, N. Mahmood, H. Yin, F. Liu and Y. Hou, Synthesis of phosphorus-doped graphene and its multifunctional applications for oxygen reduction reaction and lithium ion batteries, *Adv. Mater.*, 2013, **25**, 4932–4937.

39 S. Samanta, S. Khilari, K. Bhunia, D. Pradhan, B. Satpati and R. Srivastava, Double-Metal-Ion-Exchanged Mesoporous Zeolite as an Efficient Electrocatalyst for Alkaline Water Oxidation: Synergy between Ni–Cu and Their Contents in Catalytic Activity Enhancement, *J. Phys. Chem. C*, 2018, **122**, 10725–10736.

40 Q. Wu, M. Sadakane, H. Ogihara and W. Ueda, Immobilization of nanofibrous A- or B-site substituted

LaMnO$_3$ perovskite-type oxides on macroscopic fiber with carbon nanofibers templates, *Mater. Res. Bull.*, 2010, **45**, 1330–1333.

41 L. Wang, M.-X. Chen, Q.-Q. Yan, S.-L. Xu, S.-Q. Chu, P. Chen, Y. Lin and H.-W. Liang, A sulfur-tethering synthesis strategy toward high-loading atomically dispersed noble metal catalysts, *Sci. Adv.*, 2019, **5**, eaax6322.

42 C. M. A. Parlett, P. Keshwalla, S. G. Wainwright, D. W. Bruce, N. S. Hondow, K. Wilson and A. F. Lee, Hierarchically ordered nanoporous Pd/SBA-15 catalyst for the aerobic selective oxidation of sterically challenging allylic alcohols, *ACS Catal.*, 2013, **3**, 2122–2129.

43 Y. Li, L. Zou, J. Li, K. Guo, X. Dong, X. Li, X. Xue, H. Zhang and H. Yang, Synthesis of ordered mesoporous NiCo$_2$O$_4$ *via* hard template and its application as bifunctional electrocatalyst for Li-O$_2$ batteries, *Electrochim. Acta*, 2014, **129**, 14–20.

44 G. Li, H. Yu, W. Song, M. Dou, Y. Li, Z. Shao and B. Yi, A hard-template method for the preparation of IrO$_2$, and its performance in a solid-polymer-electrolyte water electrolyzer, *ChemSusChem*, 2012, **5**, 858–861.

45 H. Yu, F. Chu, X. Zhou, J. Ji, Y. Liu, Y. Bu, Y. Kong, Y. Tao, Y. Li and Y. Qin, A perovskite oxide with a tunable pore-size derived from a general salt-template strategy as a highly efficient electrocatalyst for the oxygen evolution reaction, *Chem. Commun.*, 2019, **55**, 2445–2448.

46 L. Yang, H. Liu, H. Shen, Y. Huang, S. Wang, L. Zheng and D. Cao, Physically adsorbed metal ions in porous supports as electrocatalysts for oxygen evolution reaction, *Adv. Funct. Mater.*, 2020, **30**, 1909889.

47 Z. Cai, L. Li, Y. Zhang, Z. Yang, J. Yang, Y. Guo and L. Guo, Amorphous nanocages of Cu-Ni-Fe hydr(oxy)oxide prepared by photocorrosion for highly efficient oxygen evolution, *Angew. Chem., Int. Ed.*, 2019, **58**, 4189–4194.

48 A. Mulderig, G. Beaucage, K. Vogtt, H. Jiang and V. Kuppa, Quantification of branching in fumed silica, *J. Aerosol Sci.*, 2017, **109**, 28–37.

49 M. Thommes, K. Kaneko, A. V. Neimark, J. P. Olivier, F. Rodriguez-Reinoso, J. Rouquerol and K. S. Sing, Physisorption of gases, with special reference to the evaluation of surface area and pore size distribution (IUPAC Technical Report), *Pure Appl. Chem.*, 2015, **87**, 1051–1069.

50 M. B. Stevens, L. J. Enman, A. S. Batchellor, M. R. Cosby, A. E. Vise, C. D. M. Trang and S. W. Boettcher, Measurement techniques for the study of thin film heterogeneous water oxidation electrocatalysts, *Chem. Mater.*, 2017, **29**, 120–140.

51 K. S. W. Sing and R. T. Williams, Physisorption hysteresis loops and the characterization of nanoporous materials, *Adsorpt. Sci. Technol.*, 2004, **22**, 773–782.

52 J. Lai, A. Nsabimana, R. Luque and G. Xu, 3D porous carbonaceous electrodes for electrocatalytic applications, *Joule*, 2018, **2**, 76–93.

53 P. Jussila, H. Ali-Löytty, K. Lahtonen, M. Hirsimäki and M. Valden, Effect of surface hydroxyl concentration on the bonding and morphology of aminopropylsilane thin films on austenitic stainless steel, *Surf. Interface Anal.*, 2010, **42**, 157–164.

54 C. Guo, J. S. Jordan, J. L. Yarger and G. P. Holland, Highly efficient fumed silica nanoparticles for peptide bond formation: converting alanine to alanine anhydride, *ACS Appl. Mater. Interfaces*, 2017, **9**, 17653–17661.

55 F. Fan, Z. Feng and C. Li, UV raman spectroscopic studies on active sites and synthesis mechanisms of transition metal-containing microporous and mesoporous materials, *Acc. Chem. Res.*, 2010, **43**, 378–387.

56 E. L. Lee and I. E. Wachs, In situ raman spectroscopy of SiO$_2$-supported transition metal oxide catalysts: an isotopic ^{18}O–^{16}O exchange study, *J. Phys. Chem. C*, 2008, **112**, 6487–6498.

57 Y. Li, Z. Feng, Y. Lian, K. Sun, L. Zhang, G. Jia, Q. Yang and C. Li, Direct synthesis of highly ordered Fe-SBA-15 mesoporous materials under weak acidic conditions, *Microporous Mesoporous Mater.*, 2005, **84**, 41–49.

58 S. Anantharaj, K. Karthick and S. Kundu, Evolution of layered double hydroxides (LDH) as high performance water oxidation electrocatalysts: A review with insights on structure, activity and mechanism, *Mater. Today Energy*, 2017, **6**, 1–26.

59 H. Xiao, H. Shin and W. A. Goddard, Synergy between Fe and Ni in the optimal performance of (Ni,Fe)OOH catalysts for the oxygen evolution reaction, *Proc. Natl. Acad. Sci. U. S. A.*, 2018, **115**, 5872–5877.

60 H. Shin, H. Xiao and W. A. Goddard, *In silico* discovery of new dopants for Fe-doped Ni oxyhydroxide (Ni1–xFe$_x$OOH) catalysts for oxygen evolution reaction, *J. Am. Chem. Soc.*, 2018, **140**, 6745–6748.

61 G. Chen, T. Wang, J. Zhang, P. Liu, H. Sun, X. Zhuang, M. Chen and X. Feng, Accelerated hydrogen evolution kinetics on NiFe-layered double hydroxide electrocatalysts by tailoring water dissociation active sites, *Adv. Mater.*, 2018, **30**, 1706279.

62 C. Luan, G. Liu, Y. Liu, L. Yu, Y. Wang, Y. Xiao, H. Qiao, X. Dai and X. Zhang, Structure effects of 2D materials on α-nickel hydroxide for oxygen evolution reaction, *ACS Nano*, 2018, **12**, 3875–3885.

63 M. Yu, S. Zhou, Z. Wang, J. Zhao and J. Qiu, Boosting electrocatalytic oxygen evolution by synergistically coupling layered double hydroxide with MXene, *Nano Energy*, 2018, **44**, 181–190.

64 X. Jia, S. Gao, T. Liu, D. Li, P. Tang and Y. Feng, Fabrication and bifunctional electrocatalytic performance of ternary CoNiMn layered double hydroxides/polypyrrole/reduced graphene oxide composite for oxygen reduction and evolution reactions, *Electrochim. Acta*, 2017, **245**, 59–68.